metals

Article

Effects of Residual Stresses on Fatigue Crack Propagation of T-Joint Using Extended Finite Element Method (XFEM)

Shizhe Chen [1], Muying Guo [1], Yicheng Li [1], Xian Dong [2] and Jianian He [1,*]

[1] School of Civil and Transportation Engineering, Guangdong University of Technology, Guangzhou 510006, China
[2] School of Civil Engineering, Shijiazhuang Tiedao University, Shijiazhuang 050043, China
* Correspondence: jnhe@gdut.edu.cn

Abstract: The welds of T-joints are prone to fatigue cracking owing to stress concentrations and welding residual stresses. Previous studies investigated the crack propagation rate using numerical simulations; however, most employed two-dimensional models and ignored the effect of residual stresses. In this study, reliable temperature and residual stress fields were obtained through numerical simulations and verified experimentally. The effects of residual stresses on crack propagation were then investigated under different loading conditions. The residual stress field caused the direction of crack propagation to shift towards the web and accelerated the crack propagation speed with increasing displacement loading.

Keywords: T-joint; residual stresses; extended finite element method; fatigue crack propagation

Citation: Chen, S.; Guo, M.; Li, Y.; Dong, X.; He, J. Effects of Residual Stresses on Fatigue Crack Propagation of T-Joint Using Extended Finite Element Method (XFEM). *Metals* **2022**, *12*, 1368. https://doi.org/10.3390/met12081368

Academic Editor: António Bastos Pereira

Received: 1 July 2022
Accepted: 15 August 2022
Published: 19 August 2022

1. Introduction

Structures subjected to cyclic loads are likely to experience fatigue damage. This is particularly true for welded structures because the rapid warming and cooling of the metal during the welding process causes uneven expansion and contraction. This phenomenon leads to permanent plastic deformation and residual stresses in the welded structure, thereby adversely affecting its integrity, durability, and appearance. Many studies have conducted fatigue tests and numerical simulations to investigate the fatigue properties of welded structures. Numerical simulations have been increasingly employed in fatigue research owing to their reproducibility, low cost, and visualisation of internal structures. The traditional method to study fatigue properties is based on the evaluation of the stress–life curve (S–N curve). However, this method possesses several drawbacks: it only considers the stage before crack initiation, ignores the initial material defects, and cannot describe the stage of fatigue crack propagation. However, initial cracks often exist in welded structures, and the crack propagation phase cannot be ignored. Therefore, an alternative method of fatigue-life assessment based on fracture mechanics was introduced to overcome these drawbacks.

The extended finite element method (XFEM) was first proposed by Belytschko and Black [1] to simulate two-dimensional (2D) crack propagation; however, later, it was applied to simulate three-dimensional (3D) crack propagation and then combined with Paris' law to simulate fatigue crack propagation. Accordingly, based on XFEM, various studies have been conducted on fatigue crack propagation and fatigue properties under different initial crack angles [2], multiple discontinuities [3], thermal cyclic loading [4,5], and residual stresses [6]. Moreover, several effective models and improvements for the XFEM [7,8] have been proposed.

The XFEM was first applied to crack propagation approximately twenty years ago [1], and its use has proliferated since because it enables the model to be independent of the mesh. Thus, the mesh does not have to be updated as the crack propagates. However, the XFEM is typically used to analyse 2D problems; it is rarely used for the fatigue analysis of

3D T-welded joints and has not to date included crack propagation analysis considering the effects of the residual stress field.

Therefore, in this study, the temperature field during the welding of a T-joint was first simulated as a simplified autogenous heat source and used as an initial condition to obtain the residual stress field, which was then verified by comparison with previous tests in the literature. The XFEM was then combined with Paris' law to analyse the crack propagation in the T-joint with and without the residual stress field as the initial stress field. The results show that the residual stress field deflected the crack propagation along the crack length and depth directions towards the web and accelerated crack propagation by an order of magnitude. This acceleration was more pronounced under high displacement loads and low-cycle fatigue. Therefore, when analysing the fatigue properties of welded structures, residual stresses can deflect the direction and considerably accelerate the rate of crack propagation, especially in structures subjected to high displacements and low-cycle fatigue.

2. Finite Element Analysis of the Welding Process

This section discusses the weld simulation analysis performed to obtain the resulting residual stresses. The simulation of the welding process can be divided into two parts: in the first part, a thermal model is used in which the heat transfer from the welding arc to the specimen is modelled using finite element analysis; in the second part, the stresses caused by temperature change are modelled.

2.1. Thermal Analysis

2.1.1. Geometry of the Model

The T-joint specimen used in this study, shown in Figure 1, is referenced from Perić [9]. The specimen consisted of two plates of thickness 15 mm and dimensions 350 mm × 150 mm. In the test from Perić's research [9], the weld was a combined weld and partially penetrated. In the welding process simulation model, due to the problem of mesh division, the weld was simplified and the fillet weld was used. Two welds were welded twice and cooled for 352 s. The plates were freely welded in a T configuration without any fixtures and secured with tack welds at each end such that the joint had a negligible gap before the beginning of the welding process. The specimens were welded using the buried-arc welding procedure. Table 1 lists the primary welding parameters used.

Table 1. Main welding parameters.

Welding Current I	Welding Voltage U	Welding Speed v	Wire Diameter	Wire Feed Speed
540 A	41 V	404 mm/min	1.6 mm	10.6 m/min

2.1.2. Material Properties

The plate material was non-alloyed low-carbon steel S355J2 + N; its temperature-dependent thermal and mechanical properties are shown in Tables 2 and 3 [10]. For any material property in Tables 2 and 3, the value for an unlisted temperature can be obtained by linear interpolation of two adjacent data points within the listed temperature range.

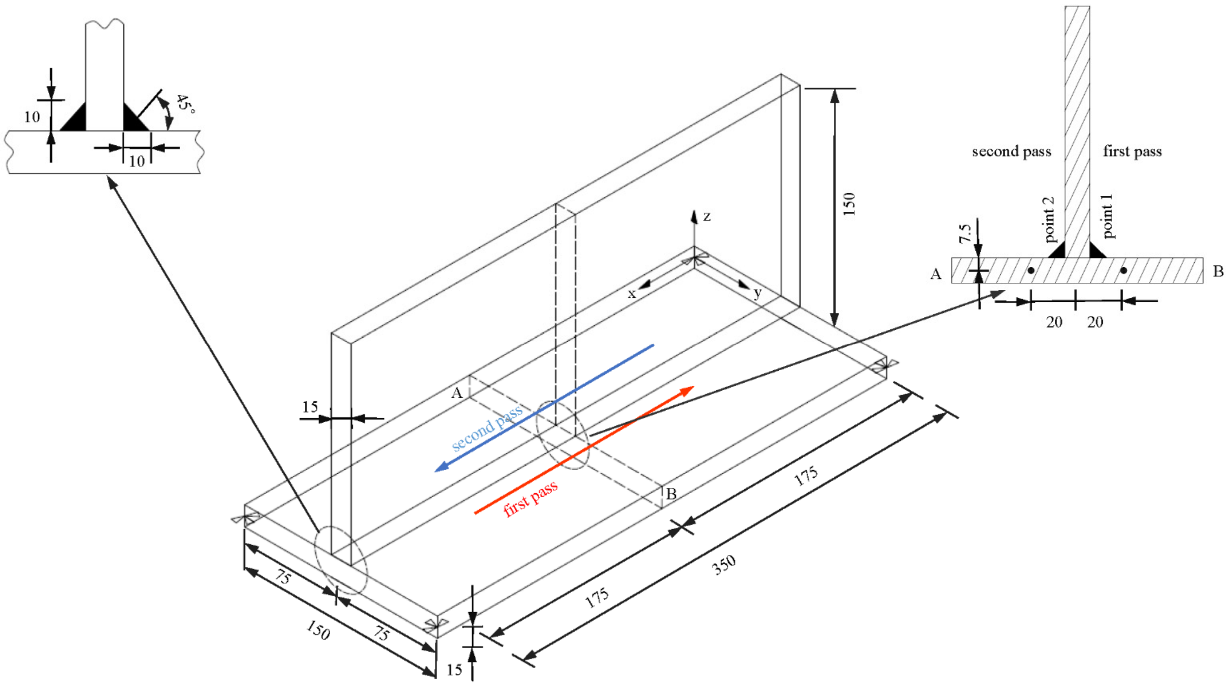

Figure 1. Geometry of the subject T-joint (unit: mm).

Table 2. Thermal properties of S355J2 + N steel.

Temperature /°C	Thermal Properties		
	Thermal Conductivity /W·m^{-1}·K^{-1}	**Density /kg·m^{-3}**	**Specific Heat /J·kg^{-1}·K^{-1}**
0	0.547	7850	0.394
700			0.894
750	0.292		1.22
800	0.257		
850			0.611
1450	0.311	7450	0.81
1500	1.095		
1600	1.103	7450	0.81

Table 3. Mechanical properties of S355J2 + N steel.

Temperature /°C	Mechanical Properties			
	Yield Stress /MPa	**Modulus of Elasticity /GPa**	**Thermal Expansion Coefficient /10^{-5} °C^{-1}**	**Poisson's Ratio**
0	345	206	1.217	0.307
100	332	204		0.321
200	308	201		0.335
300	278	201		0.353
400	234	164		0.385
500	188	100		0.385
600	128	61		0.398
700	69	42		0.416
800	66	30		0.448
900	46	21		0.480
1000	12	11		0.480
1450	12	11	1.412	0.480
1600	12	11	1.412	0.480

2.1.3. Heat Input Model

In the welding process simulation model, the temperature of the specimen was modelled using a transient thermal analysis in Abaqus. The thermal processes associated with welding can be divided into three components: heat input from the welding arc, heat transfer through the specimen, and heat loss to the environment. The governing equation for the thermal model is given by:

$$\frac{\partial}{\partial x}\left(k\frac{\partial T}{\partial x}\right)+\frac{\partial}{\partial y}\left(k\frac{\partial T}{\partial y}\right)+\frac{\partial}{\partial z}\left(k\frac{\partial T}{\partial z}\right)+Q=\rho C\frac{\partial T}{\partial t} \tag{1}$$

where T is the temperature, t is the time, ρ is the density, C is the specific heat capacity, Q is the internal heat-generation rate, and k is the thermal conductivity. Equation (1) is a nonlinear differential equation because, parameters ρ, C, and k depend on the temperature, which changes over time. The initial temperature and boundary conditions of the problem are as follows:

$$T(x,y,z,0)=T_0(x,y,z) \tag{2}$$

$$q=-k\left(\frac{\partial T}{\partial x}+\frac{\partial T}{\partial y}+\frac{\partial T}{\partial z}\right) \tag{3}$$

where q denotes the heat flux at the boundary. There are typically three ways to transfer heat during welding: heat conduction, thermal convection, and thermal radiation, which can be, respectively, calculated using:

$$q=-kA\frac{\partial t}{\partial n} \tag{4}$$

$$q_2=h(T_S-T_F) \tag{5}$$

$$q_3=\varepsilon\sigma F_{12}\left(T_1^4-T_2^4\right) \tag{6}$$

where $\partial t/\partial n$ is the temperature gradient, h is convective heat transfer coefficient, T_S is the solid surface temperature, T_F is the fluid temperature, ε is the heat absorption rate, σ is the Stefan–Boltzmann constant, F_{12} is the radiation surface shape factor, and T_1 and T_2 are the absolute temperatures of radiation surfaces 1 and 2, respectively.

In the case of low-carbon steel welding, phase changes need not be considered because they have little effect on the residual stress field and deformation [11]. In addition, owing to the short duration of the high-temperature cycle during welding, the creep effect of the material is minimal and can be neglected. Commonly used double ellipsoidal [12] and Gaussian [13] heat sources need to be combined with experimental data to adjust the associated parameters. A simplified definition of heat flux was used in the thermal analysis conducted in this study by assuming that the total heat input to the weld flows through the molten droplets and that the heat flux is uniformly distributed over the volume of the weld. The heat flux during welding is given by

$$Q=\frac{\eta UI}{V_H} \tag{7}$$

where Q is the effective power for welding, η is the efficiency of the welding process, V_H is the heat-source volume, and U and I are the welding voltage and current, respectively. The efficiency of the welding process simulated in this study was estimated to be approximately 80% [14], and the heat flux introduced to the weld was therefore $Q=9.7\times10^{10}\mathrm{J{\cdot}m^{-3}{\cdot}s^{-1}}$. A convective heat transfer coefficient $h=10\mathrm{W{\cdot}m^{-2}{\cdot}K^{-1}}$ and an emissivity $\varepsilon=0.9$ were assumed for the outer surfaces of the welded model [15].

2.1.4. FEM Model Details

A finite element mesh of the T-joint specimen consisting of 27,450 elements is shown in Figure 2. Heat conduction element, with a separate degree of freedom to define the temperature, was selected as the element type of this model. An extremely dense mesh was created in the weld pool and surrounding area, where the thermal gradient will be the largest; in the area away from the weld, where the thermal gradient will be smaller, a coarser mesh was used to reduce the total number of elements. A commonly used finite element mesh transition technique was employed to connect meshes of different scales, as illustrated in Figure 3. In the analysis, the electrode movement and weld filler addition were simulated by applying the element birth and death technique. Thus, no weld material was present at the beginning of the analysis, and the necessary weld elements were activated in the model as the thermal analysis simulation progressed. To simulate the movement of the electrode, the weld bead was divided into 180 element sets, each 3.89 mm in length. Each step was defined for the electrode movement and weld filler addition of each element set. For each of these steps, the time is 0.5 s, the initial increment step is 0.05, the maximum increment step is 0.5, and the maximum temperature change in each increment step is 1500 °C. Before the analysis started, all the weld elements were deactivated using the 'model change' command in Abaqus to define them as 'dead' weld elements. These dead elements were sequentially reactivated using the 'model change' command as the weld progressed, resulting in the 'birth' of each element as the heat source moved over it in the model. This simultaneously simulated the heat input from the arc and the deposition of the weld material on the specimen. Two cooling analysis steps were carried out, one between the two welding processes, and the other after the second welding.

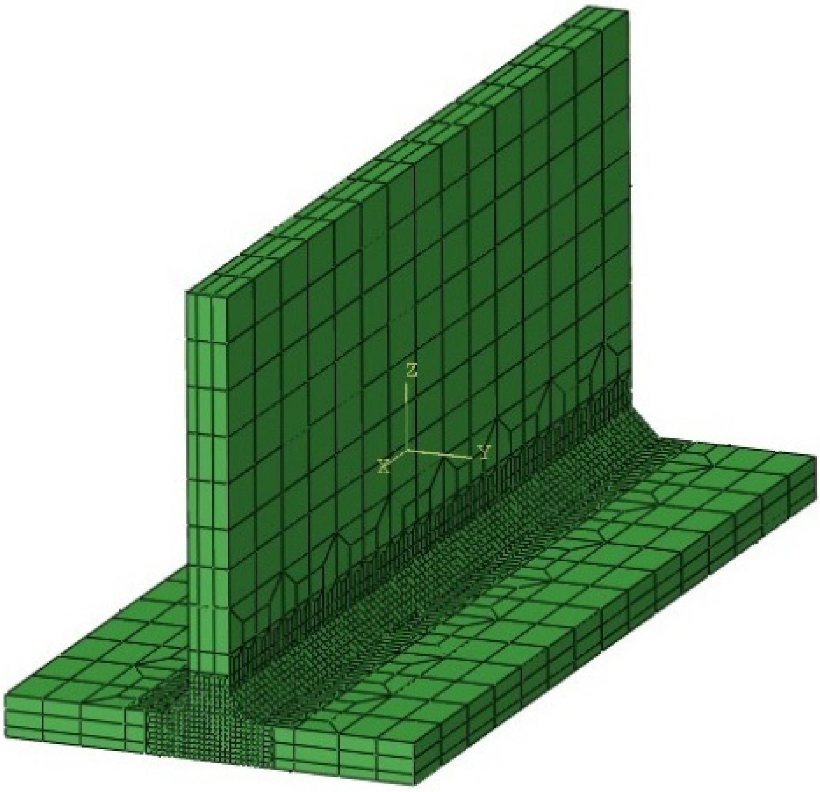

Figure 2. Finite element mesh of the T-joint specimen.

2.1.5. Results of Welding Simulation

The results of the welding simulation provided the temperature field data at every time step over the entire model. The molten zone of the weld is shown in Figure 4, assuming that the steel material melts at approximately 1600 °C; temperatures greater than 1600 °C are shown in light grey. This zone was confirmed to be reasonable by comparison with the results of other studies. Figure 5 shows a comparison of the simulated and measured temperature history at points 1 and 2 in the A–B cross-section (Figure 1) during the first 800 s of welding. The first weld was applied and cooled in the first 400 s, and then the second one was applied and also cooled in the next 400 s. It can be observed that the numerically simulated temperature history trends are in good agreement with the experimental results. However, the temperatures obtained by the numerical simulation were lower than those obtained during the experiment. This can be attributed to three reasons.

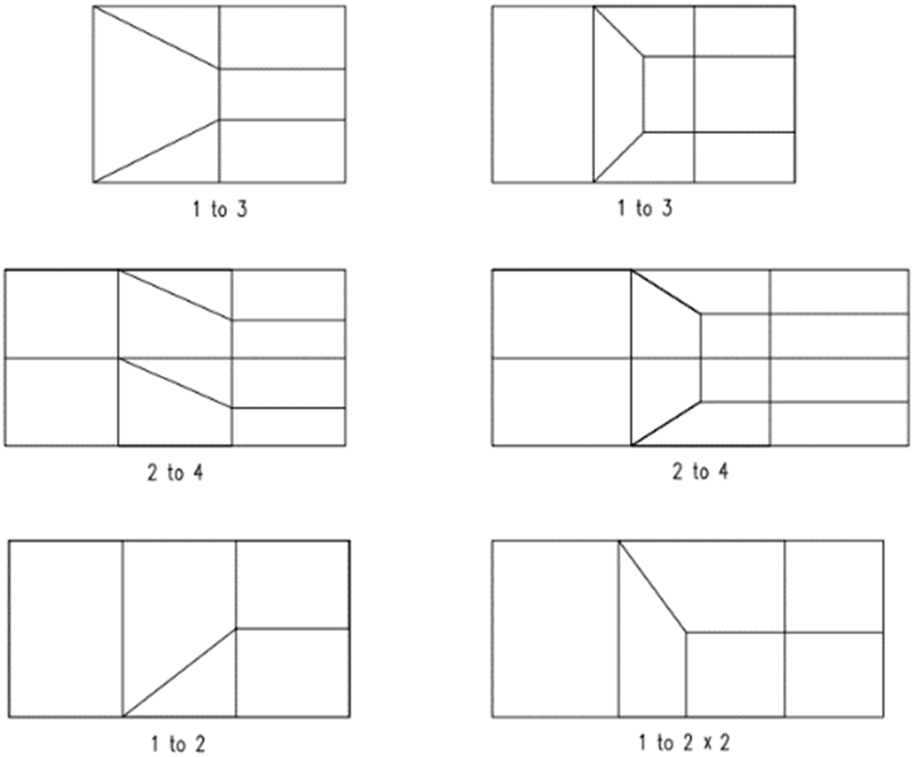

Figure 3. Finite-element mesh transition techniques.

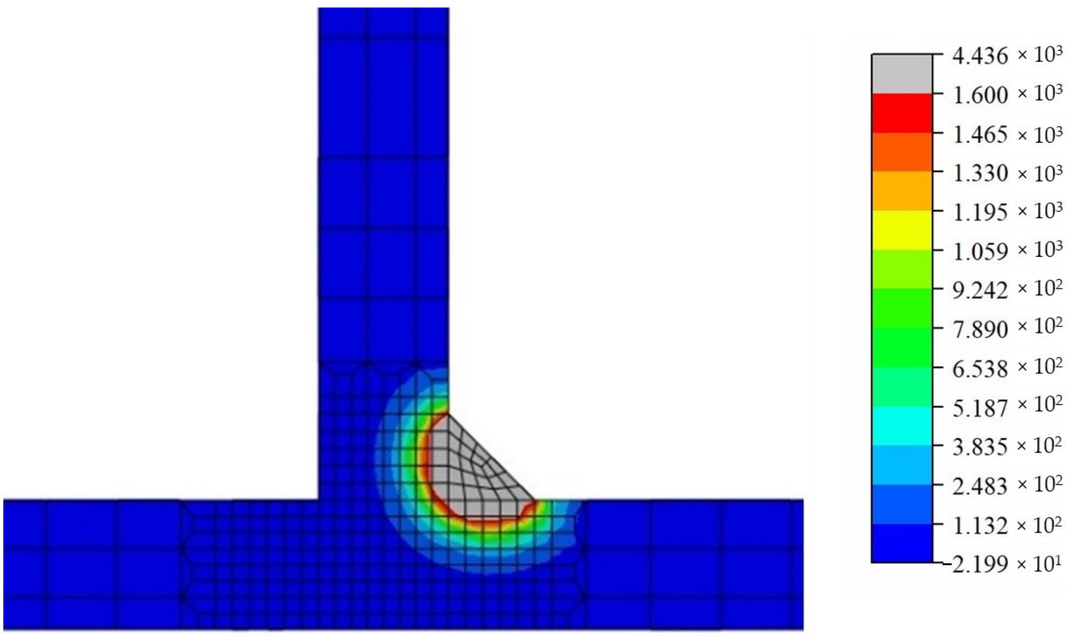

Figure 4. Molten zone of the weld (unit: °C).

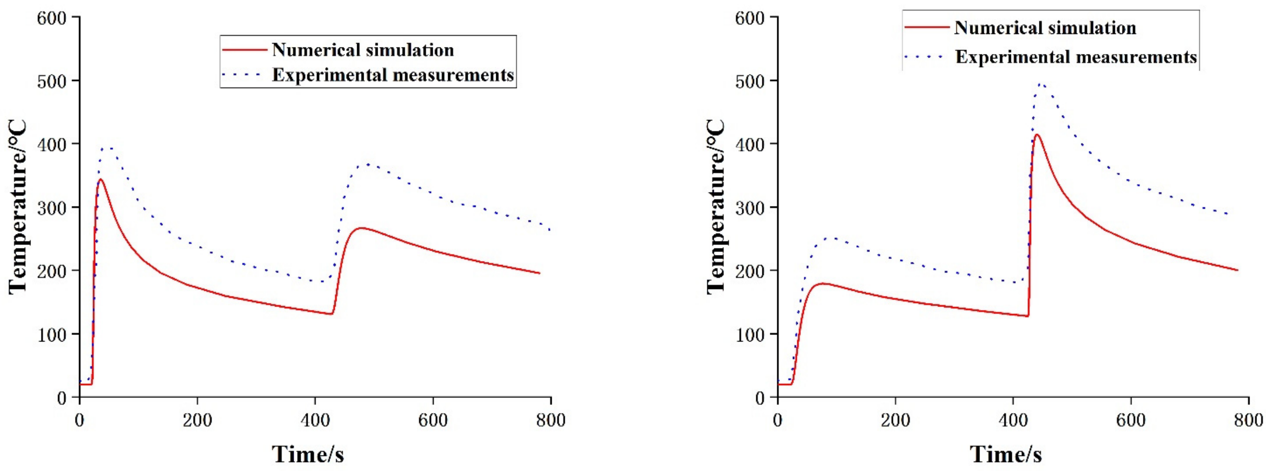

(**a**) (**b**)

Figure 5. Temperature–time histories at the nodes: (**a**) Point 1; (**b**) Point 2.

(1) Simplified models were employed in this study to simulate the heat flux distribution and thermal boundary conditions using a uniform value per weld volume; in a real welding scenario, the heat flux distribution is more complex and uneven.
(2) The convective heat transfer and emissivity coefficients were assumed to be constant, whereas in reality, these values are affected by the temperature.
(3) Owing to the effect of the finite element meshing, the simulation did not use the same measurement points as the test.

The full-field temperature distributions simulated 400 and 800 s after the start of the welding process are shown in Figure 6.

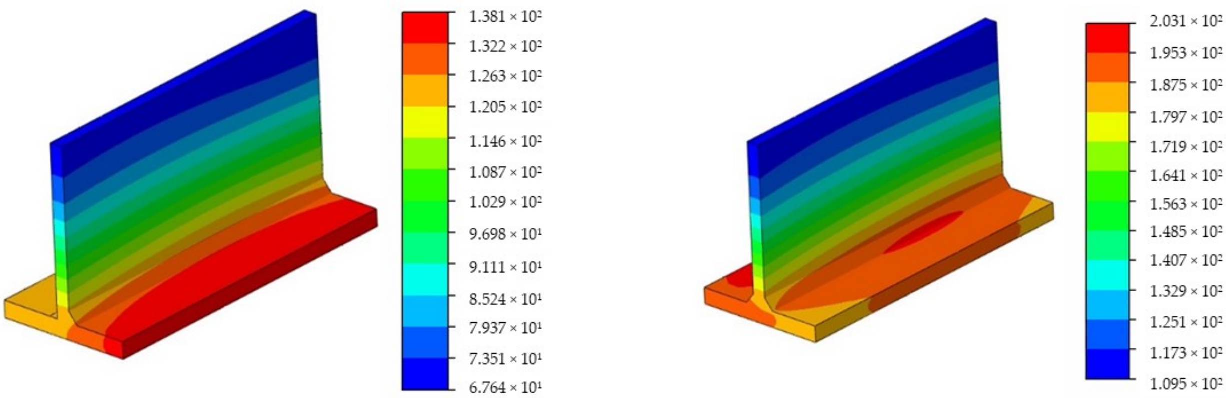

(**a**) (**b**)

Figure 6. Transient temperature field: (**a**) 400 s and (**b**) 800 s after the start of the welding process (unit: °C).

2.2. Mechanical Analysis

The residual stresses in the welds were simulated and analysed to establish a basis for the subsequent numerical fracture mechanics analysis. To facilitate the introduction of residual stress fields, the mesh generation of the residual stress analysis model was aligned with the solid part of the crack growth model. During the analysis, temperature field data were used as input to generate the intended field. The same time steps were applied in the mechanical analysis as in the thermal analysis.

2.2.1. Boundary Conditions

The mechanical boundary conditions will significantly influence the stress distribution and formation of the residual stress field [16]. However, little information is available regarding appropriate boundary conditions during the welding process. Therefore, the actual welding situation was replicated used the fewest boundary conditions possible to avoid excessive constraints that could introduce inaccuracies in the residual stress simulation and to ensure computational convergence.

2.2.2. Results of Residual Stress Simulation

Perić [9] measured the residual stresses in a welded specimen at a depth of 0.015 mm using X-ray diffraction and a drilling method. Thus, Figure 7 shows the longitudinal residual stress distributions (Figure 1, lines A–B) obtained using the numerical simulations, X-ray diffraction at a depth of 0.015mm, and the hole-drilling method. In general, the longitudinal residual stresses measured using X-ray diffraction can be observed to follow the same trend as those obtained from the numerical simulations. In the area close to the weld, the longitudinal residual stresses are all tensile, with a maximum value close to the yield strength of the base material, whereas away from the weld area, the longitudinal residual stresses change from tensile to compressive. Generally, the longitudinal residual stress distribution exhibits an Ω shape. The transverse residual stress distributions (Figure 1, lines A–B) obtained by the numerical simulation, X-ray diffraction at a depth of 0.015 mm, and the hole-drilling method are presented in Figure 8. Similar to the longitudinal stresses, the trends of the numerical simulation and experimental measurements are in agreement although the stress values from numerical simulation are higher than those of X-ray detection. Compared with the study of Perić [9], the yield strength of the steel in the finite element simulation from our research was slightly higher than that of the actual. In addition, the temperature difference of the finite element simulation was a little larger than that in reality. These factors resulted in the high residual stress. The numerically obtained full-field longitudinal and transverse residual stress distributions are shown in Figure 9.

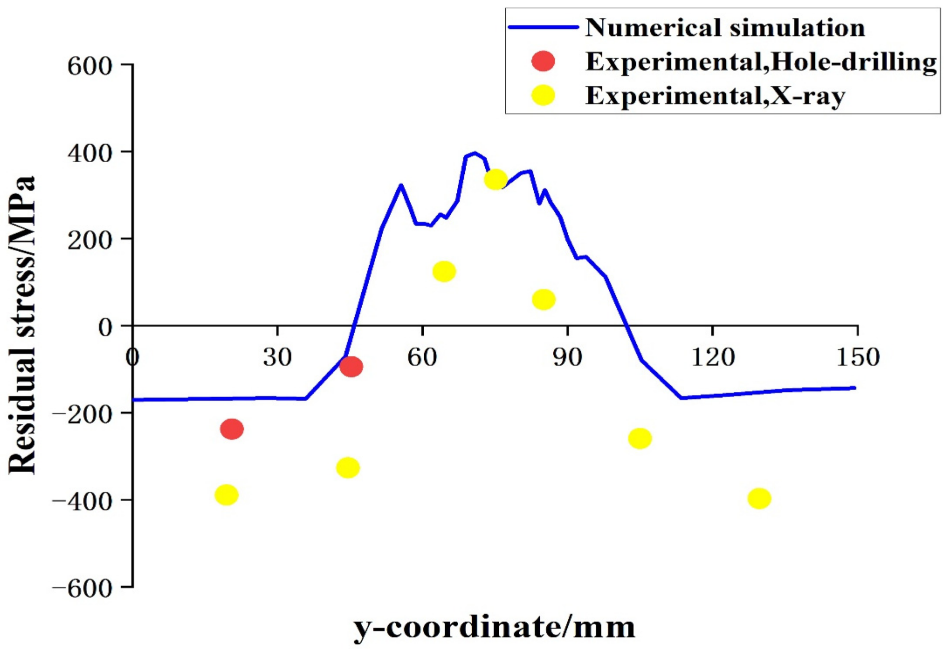

Figure 7. Longitudinal residual stress distributions (Figure 1, lines A–B) obtained using the numerical simulation, X-ray diffraction, and hole-drilling method.

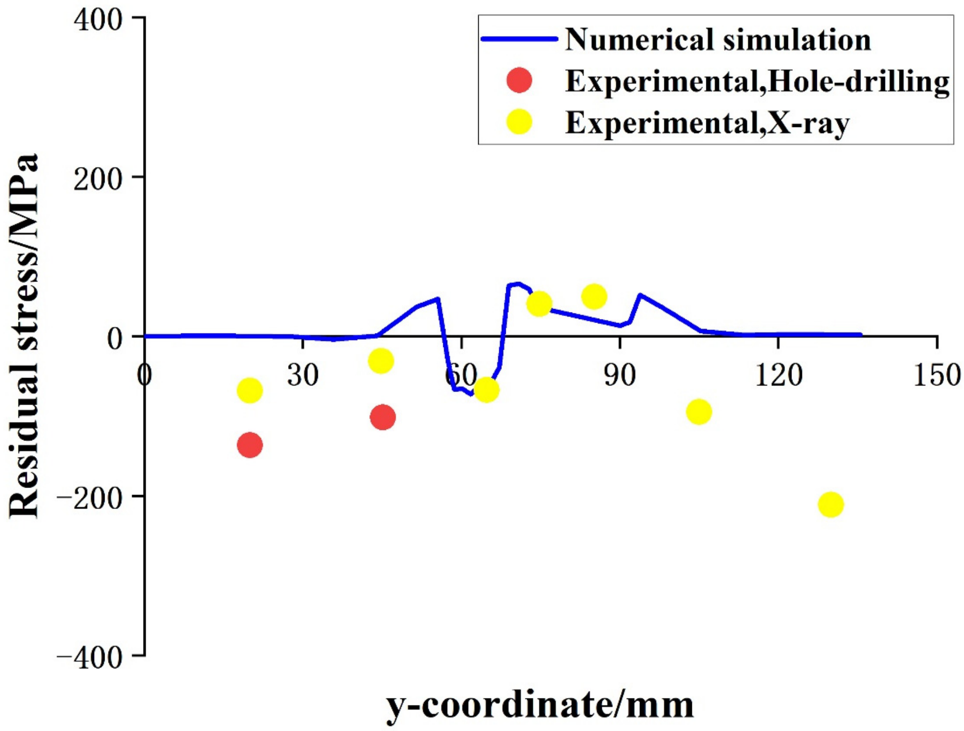

Figure 8. Transversal residual stress (Figure 1, lines A–B) obtained using X-ray diffraction at several electropolishing depths.

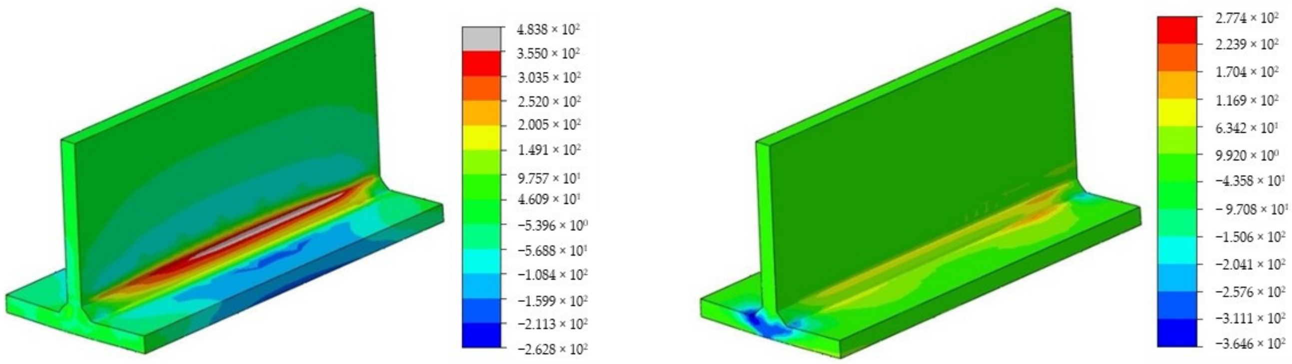

(**a**) (**b**)

Figure 9. Numerically obtained full-field residual-stress distributions in the (unit: MPa): (**a**) longitudinal residual stress field; (**b**) transversal residual stress field.

3. Fatigue Crack Simulation

In this section, the obtained residual stress field is introduced as the initial stress, and the XFEM and Paris' law are used to simulate the fatigue crack propagation.

3.1. Numerical Fracture Mechanics Analysis Theory for Crack Propagation

3.1.1. XFEM

Modelling stationary discontinuities such as cracks using the conventional finite element method requires that the mesh conform to geometric discontinuities, making the creation of a compliant mesh difficult. Modelling a growing crack is even more problematic in this approach because the mesh must be constantly updated to conform to the discontinuous geometry developed as the crack propagates. The XFEM alleviates the need to create compliant meshes so that the mesh need not be updated as the crack progresses. It is an extension of the conventional finite element method, based on the concept of partition of unity by Melenk and Babuska [17], that enables local enrichment functions to be easily incorporated into the finite element approximation. The existence of discontinuities is guaranteed by the special enrichment function, together with extra degrees of freedom. An extended finite element displacement function is used in the element shape function to reveal the discontinuity, and can be expressed as follows [18]:

$$u = \sum_{I=1}^{N} N_I(x)\left[u_I + H(x)a_I + \sum_{\alpha=1}^{4} F_\alpha(x)b_I^\alpha\right] \tag{8}$$

where $N_I(x)$ denotes the typical nodal shape function, the first term in the brackets (u_I) is the typical nodal displacement vector associated with the continuous part of the finite element solution, the second term is the product of the nodal enriched degree of freedom vector (a_I) and associated discontinuous jump function ($H(x)$) across the surfaces of the crack, and the third term is the product of the nodal-enriched degree of freedom vector (b_I^α) and associated elastic asymptotic crack-tip function ($F_\alpha(x)$). The first term on the right-hand side applies to all nodes in the model, the second is valid for nodes whose shape function supports being cut by the inner side of the crack, and the third is only used for nodes whose shape functions support being cut by the tip of the crack. Figure 10 illustrates the discontinuous jump function across the surfaces of the crack ($H(x)$), which is given by

$$H(x) = \begin{cases} 1, & \text{if } (x - x^*)\cdot n \geq 0 \\ -1, & \text{otherwise} \end{cases} \tag{9}$$

where x is a sample (Gauss) point, x^* is the point on the crack closest to x, and n is the outwards unit normal to the crack at x^*. Figure 10 illustrates the asymptotic crack tip functions ($F_\alpha(x)$) in an isotropic elastic material, calculated as follows:

$$F_\alpha(x) = \left[\sqrt{r}\sin\frac{\theta}{2}, \sqrt{r}\cos\frac{\theta}{2}, \sqrt{r}\sin\theta\sin\frac{\theta}{2}, \sqrt{r}\sin\theta\cos\frac{\theta}{2}\right] \tag{10}$$

where (r, θ) is a polar coordinate system that has its origin at the crack tip and $\theta = 0$ is the tangent to the crack at the tip. Equation (10) span the asymptotic crack-tip function of elastostatics, and $\sqrt{r}\sin(\theta/2)$ considers the discontinuity across the crack face.

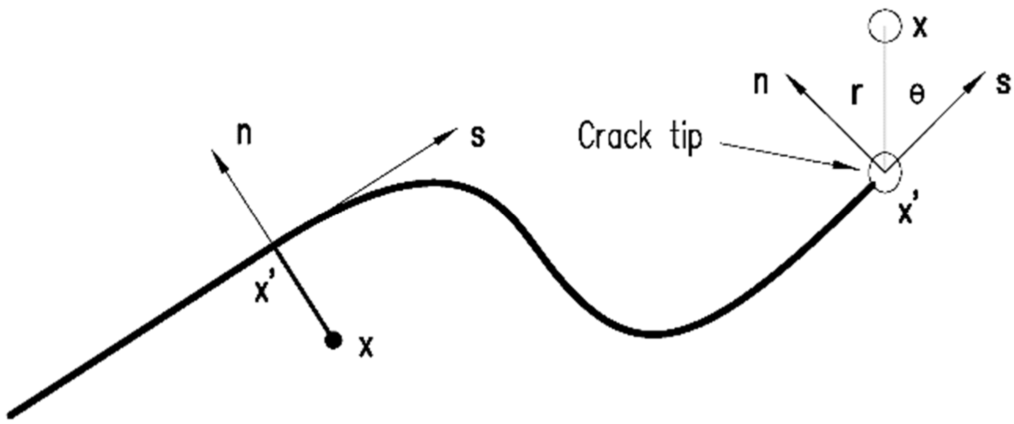

Figure 10. Illustration of normal and tangential coordinates for a smooth crack.

3.1.2. Simulation Method of Fatigue Crack Propagation

Abaqus uses the direct cyclic method for fatigue analysis simulations of fatigue crack propagation under cyclic loading. The direct cyclic method is a computational method that combines the quasi-Newton method, Fourier series representation, and residual vector to solve the response of a structure under cyclic loading. Solving nonlinear equations using this method is less computationally intensive than solving them using the full Newtonian method. In linear elastic fracture mechanics (LEFM) theory and the virtual crack closure technique (VCCT), the Paris equation is commonly used to analyse the fatigue crack extension under cyclic loading; it is expressed as follows [19]:

$$\frac{da}{dN} = C(\Delta K)^m \tag{11}$$

where a is the crack length, N is the cycle number, $\mathrm{d}a/\mathrm{d}N$ is the crack growth rate, C and m are material constants, and ΔK is the stress intensity factor amplitude. In Abaqus, the Paris equation is expressed in terms of the crack propagation and energy release rates, as follows:

$$\frac{da}{dN} = c_1 \Delta G^{c_2} \tag{12}$$

where ΔG is the strain energy release rate amplitude and c_1 and c_2 are material parameters set to extremely low values to immediately begin crack growth. According to the relationship between the energy release rate (G) and stress intensity factor (K) in the LEFM, Equation (11) can be converted into Equation (12) and expressed as:

$$G = \begin{cases} \frac{K^2}{E}, & \text{plane stress} \\ \frac{(1-v^2)K^2}{E}, & \text{plane strain} \end{cases} \tag{13}$$

where v is Poisson's ratio and E is the elastic modulus of the material.

The fatigue crack growth in the Paris regime is only possible when the following condition in Equation (14) is met:

$$G_{\text{thresh}} < \Delta G < G_{\text{pl}} \tag{14}$$

where G_{thresh} and G_{pl} are the threshold and upper limit values of the energy release rate, respectively. If the condition in Equation (14) is met, the following equation can be used to determine whether fatigue crack growth has begun:

$$f = \frac{N}{c_1 \Delta G^{c_2}} \geq 1.0 \tag{15}$$

Thus, as shown in Figure 11, the Paris regime is bounded by the energy release rate threshold (G_{thresh}), below which there is no consideration of fatigue crack initiation or growth, and the energy release rate upper limit (G_{pl}), above which the fatigue crack grows at an accelerated rate. Defining G_c as the critical Mode I energy release rate, the values of G_{thresh}/G_C and G_{pl}/G_C must be determined in conjunction with the experiment. Default values of $G_{\text{thresh}}/G_C = 0.01$ and $G_{\text{pl}}/G_C = 0.85$ were used in this study. If the amount of energy in the element is greater than G_{thresh}, the element cracks.

Stable crack growth in an element was calculated using:

$$\frac{da}{dN} = c_3 \Delta G^{c_4} \tag{16}$$

where c_3 and c_4 are material parameters.

After an element cracked, the stress field was recalculated and the next element to crack was calculated. Elements in the enriched region cracked first and required the least number of cycles. This process was repeated, and each step led to the expansion of an element over a certain number of load cycles.

The value of G_c can be specified using various mixed-mode models in Abaqus. The power law, was used to do so in this study as follows:

$$\frac{G_{eq}}{G_{eqC}} = \left(\frac{G_I}{G_{IC}}\right)^{a_m} + \left(\frac{G_{II}}{G_{IIC}}\right)^{a_n} + \left(\frac{G_{III}}{G_{IIIC}}\right)^{a_0} \tag{17}$$

where G_I, G_{II}, G_{III} are the Mode I, II, III energy release rates; $G_{IC}, G_{IIC}, G_{IIIC}$ are the critical Mode I, II, III energy release rates; G_{eq} is the equivalent strain energy release rate calculated at a node; G_{eqC} is the critical equivalent strain energy release rate calculated based on the user-specified mode-mix criterion and bond strength of the interface; and a_m, a_n and a_o are exponents. In this study, $a_m = a_n = a_o = 1$.

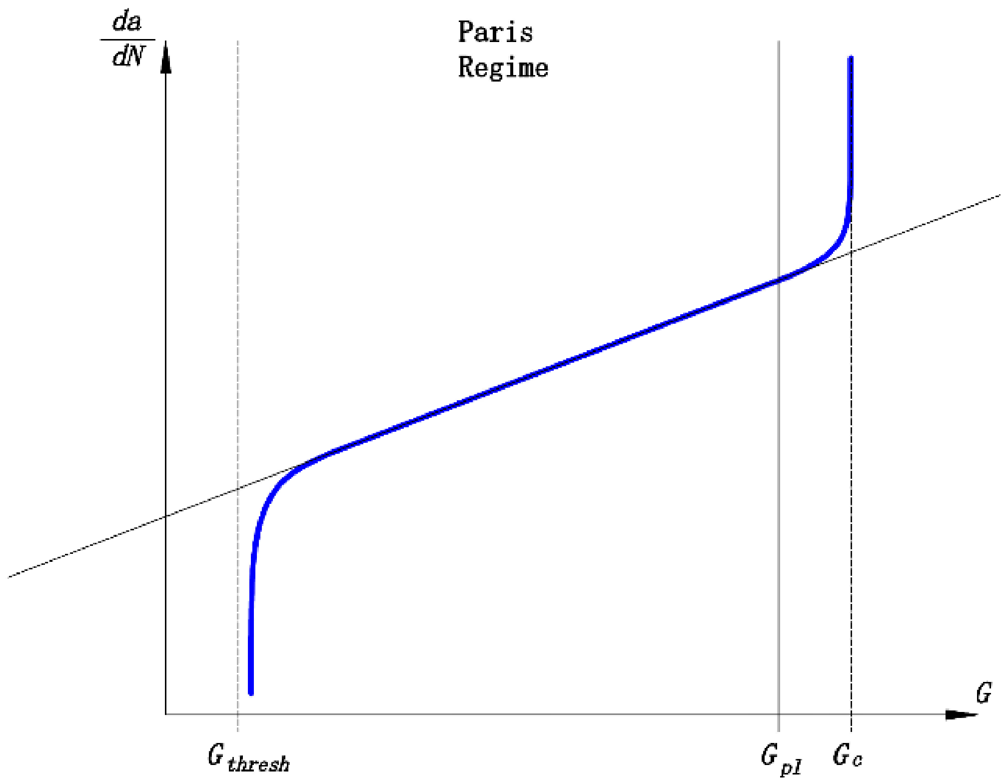

Figure 11. Fatigue crack growth governed by the Paris law.

The crack propagation procedure, based on a combination of Paris' law and the VCCT, is illustrated in Figure 12. In this procedure, the VCCT was applied to compute the amount of energy required to propagate the crack. If the amount of energy was higher than G_{thresh}, the element was considered to crack. The stable crack growth of the element was then calculated using Paris' law, from which the propagation direction, propagation length (Δa_k), and cyclic number increment (ΔN_k) were computed. Subsequently, the crack length (Δa_i) is updated as $\Delta a_i + \Delta a_k$, and the cycle number (ΔN_i) was updated as $\Delta N_i + \Delta N_k$. After an element cracked, the stress field was recalculated and the next element to crack was calculated based on the VCCT and Paris' law. The elements in the enriched region cracked first and required the least number of cycles. This process was repeated; each step corresponded to the propagation of the crack though an element over a certain number of load cycles.

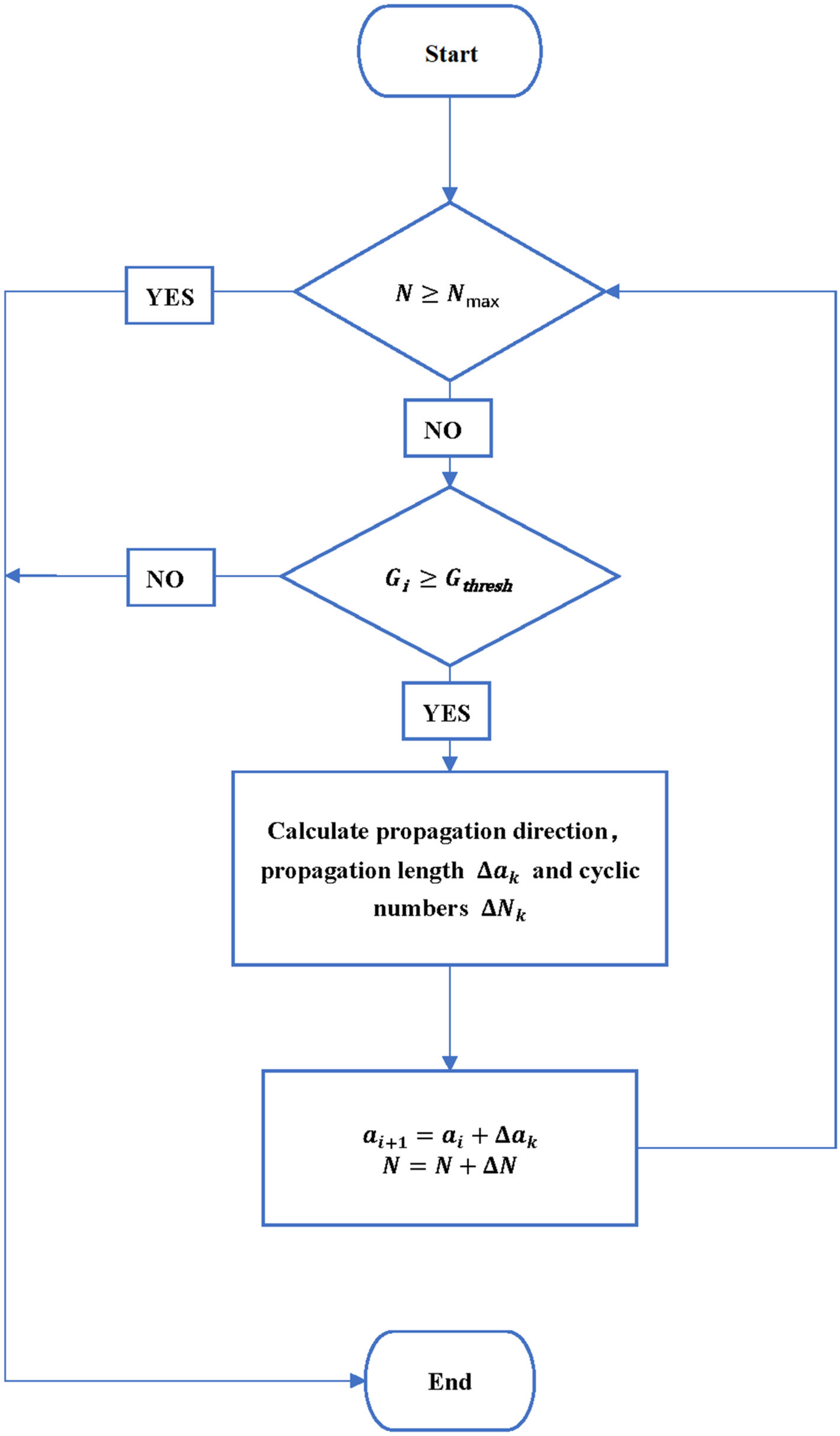

Figure 12. Illustration of XFEM propagation progress.

3.2. Loading Model and Material Properties

A crack extension analysis was performed in Abaqus using the direct-cycle method. Periodic displacement loads of 0.3, 0.35, 0.4, and 0.5 mm were applied to the model using the cyclic function shown in Figure 13, in which one full cycle requires one second. Only the elastic material properties E = 206 GPa and v = 0.3 were used for the crack extension analysis. The parameters related to Paris' law were adjusted according to the relevant literature [20,21], as shown in Table 4.

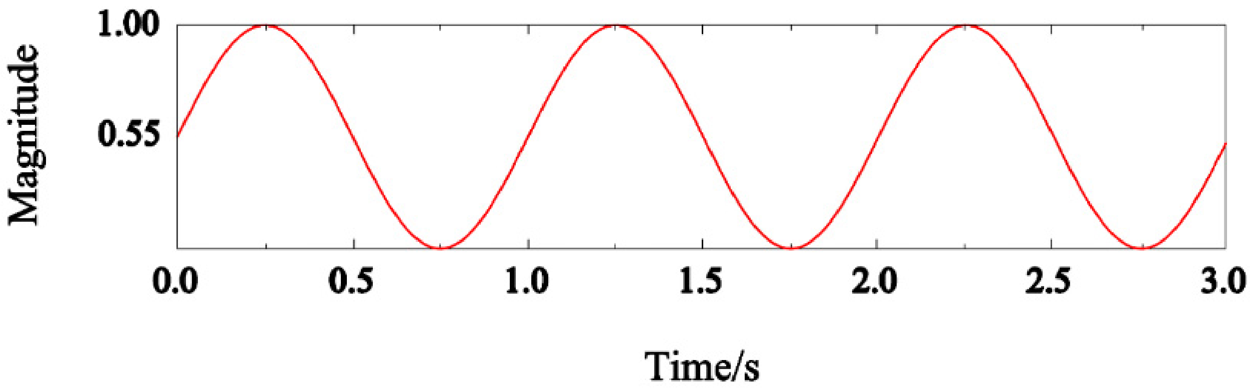

Figure 13. Direct cycle time.

Table 4. Paris law parameters.

c_3	c_4	G_I	G_{II}	G_{III}	$a_{m/n/o}$
3.0×10^{-5}	1.5	6.5	6.5	6.5	1

4. Results and Discussion

4.1. Crack Propagation

The initial crack was assumed to be semi-elliptical with a semi-short axis length (a) to long axis length ($2c$) ratio of 2.5 mm/10 mm. It was located at the mid-length toe of the first weld, as shown in Figure 14. The propagation patterns of cracks in the length and thickness directions with and without the residual stress field are shown in Figures 15–18 (Figure 1, lines A–B). When displacement loads of 0.4 mm and 0.5 mm were applied, the simulation terminated before completing 100,000 cycles owing to the specificity of the XFEM; that is, the crack propagation path could not pass through the cell nodes.

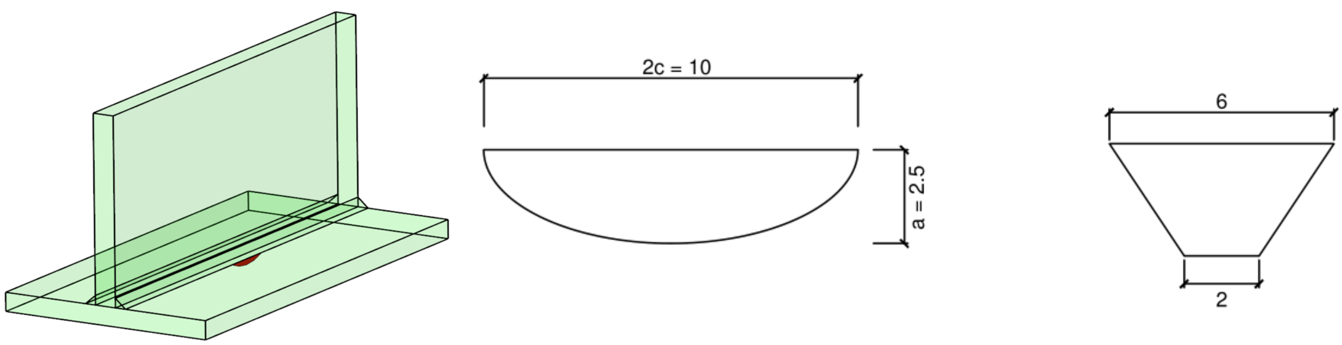

(**a**) (**b**)

Figure 14. Initial Crack Location and Shape: (**a**) Crack Location; (**b**) Crack Shape (unit: mm).

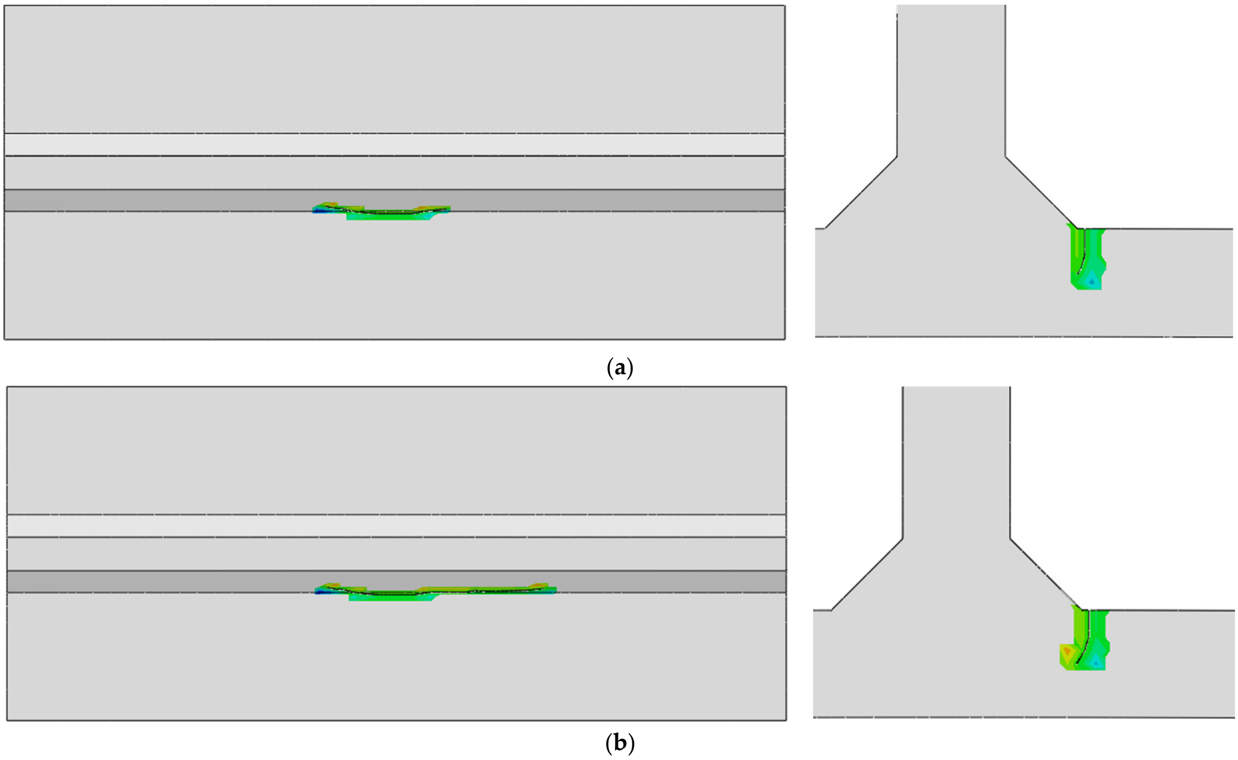

Figure 15. Crack propagation under a maximum displacement load of 0.3 mm: (**a**) without residual stress field at 100,000 cycles; (**b**) with residual stress field at 100,000 cycles.

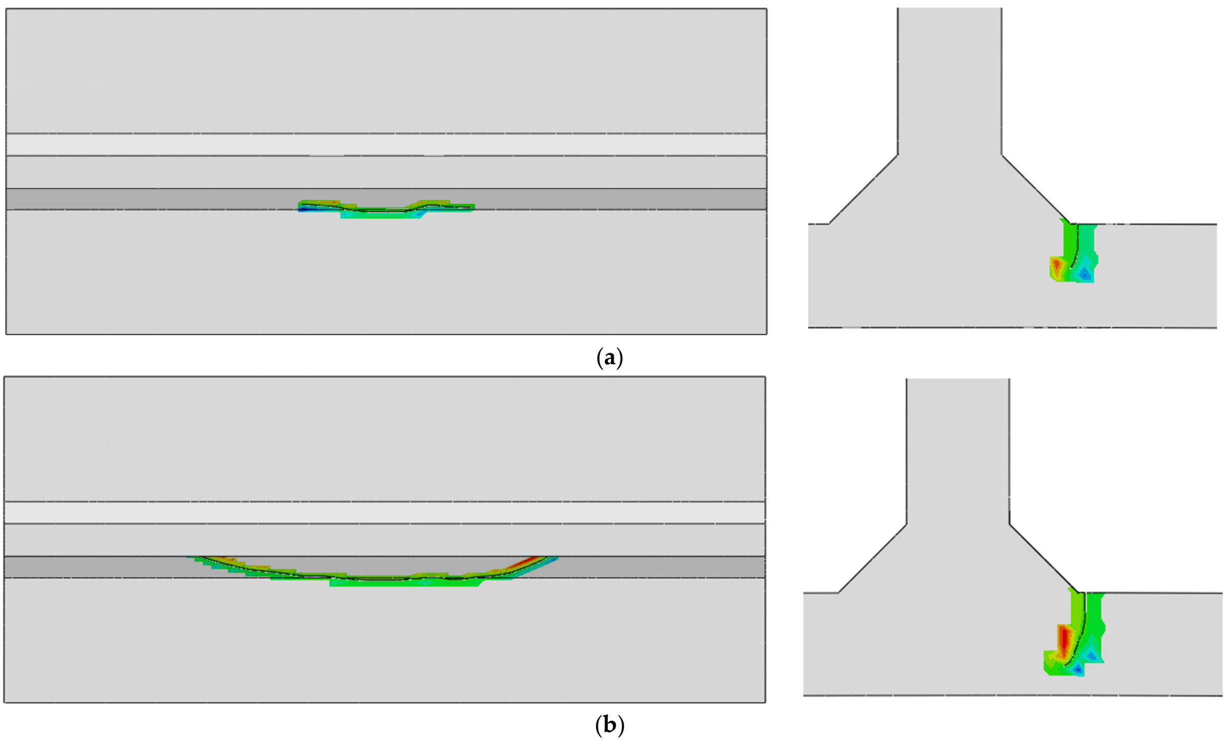

Figure 16. Crack propagation under a maximum displacement of 0.35 mm: (**a**) without residual stress field at 100,000 cycles; (**b**) with residual stress field at 100,000 cycles.

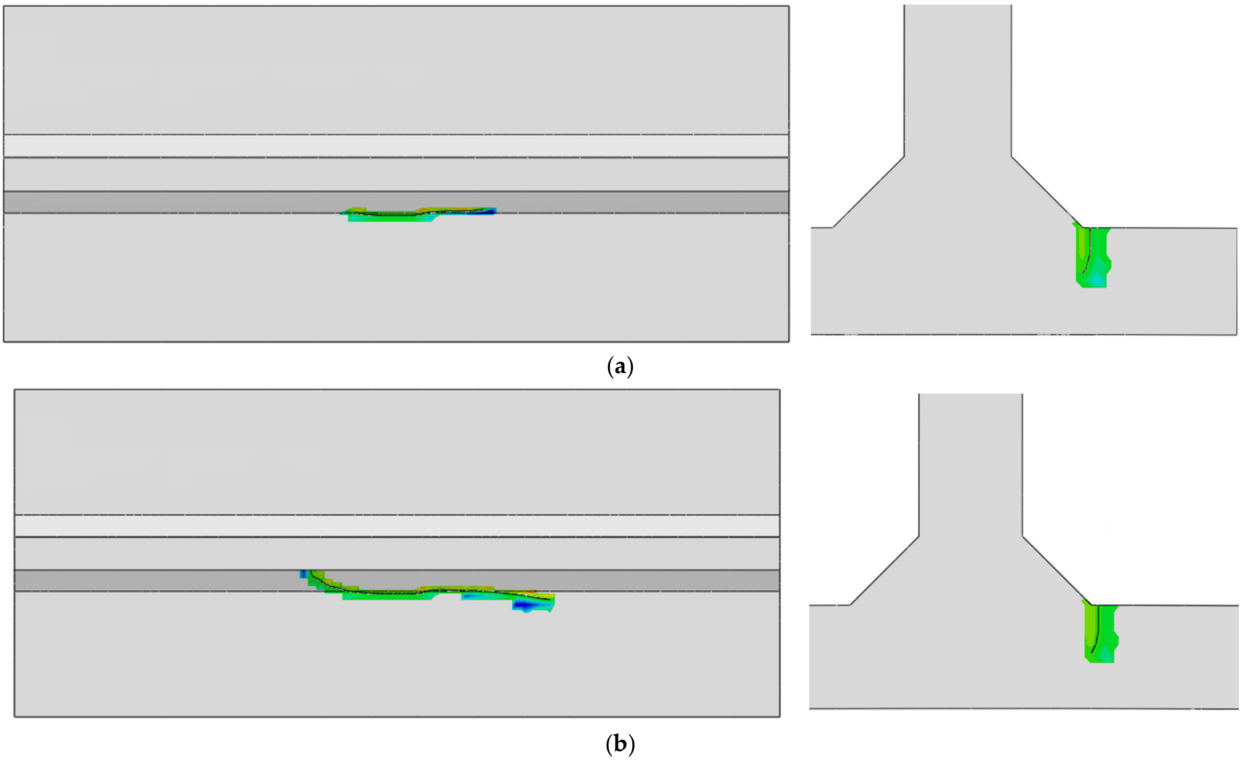

Figure 17. Crack propagation under a maximum displacement of 0.4 mm: (**a**) without residual stress field at 31,514 cycles; (**b**) with residual stress field at 9618 cycles.

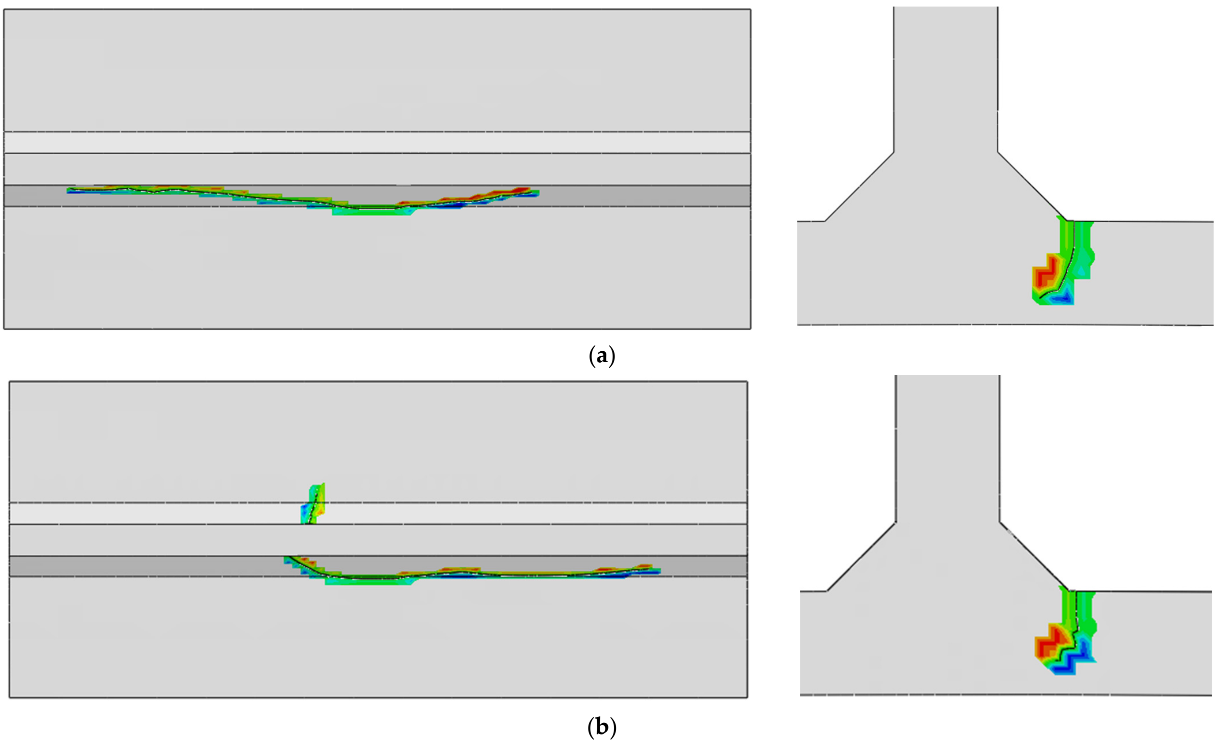

Figure 18. Crack propagation under a maximum displacement of 0.5 mm: (**a**) without residual stress field at 14,653 cycles; (**b**) with residual stress field at 37 cycles.

As shown in Figures 15–18, when there is no residual stress field, the crack propagates in the length direction along the weld. With the residual stress field, the crack propagation path begins to deflect in the direction of the web and is more noticeable under larger loading displacements. Thus, under the applied displacement loads, the crack propagation path passed directly through the web. Furthermore, the crack propagation in the thickness direction without the residual stress field was approximately orthogonal to the surface, whereas the crack propagation with the residual stress field deflected to form a 'J' shape. Clearly, the crack propagated for a much shorter length and depth without the residual stress field than with the residual stress field. Indeed, the number of damaged elements was recorded according to the applied cycle count, as shown in Figures 19–21, and their relationship can be used to approximate the crack propagation rate.

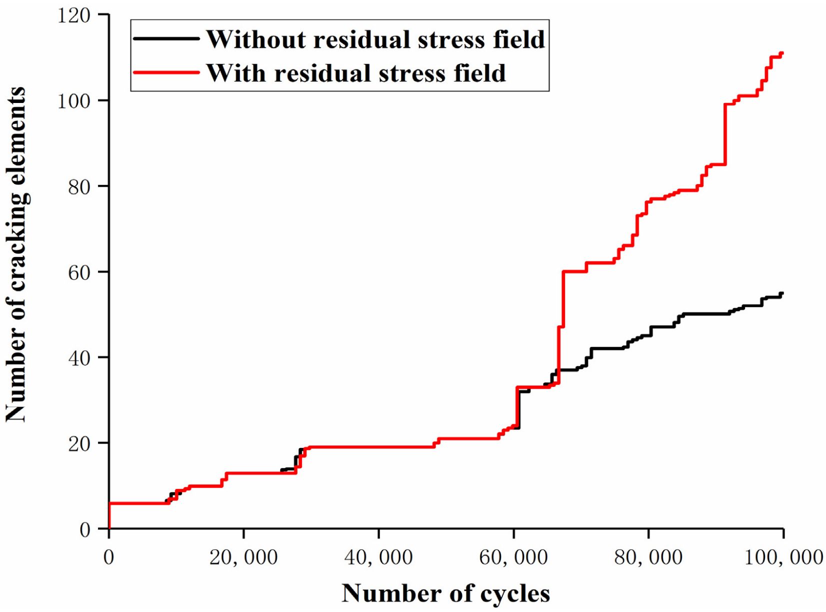

Figure 19. Relationship between the number of cracked elements and number of load cycles for with a maximum displacement load of 0.3 mm.

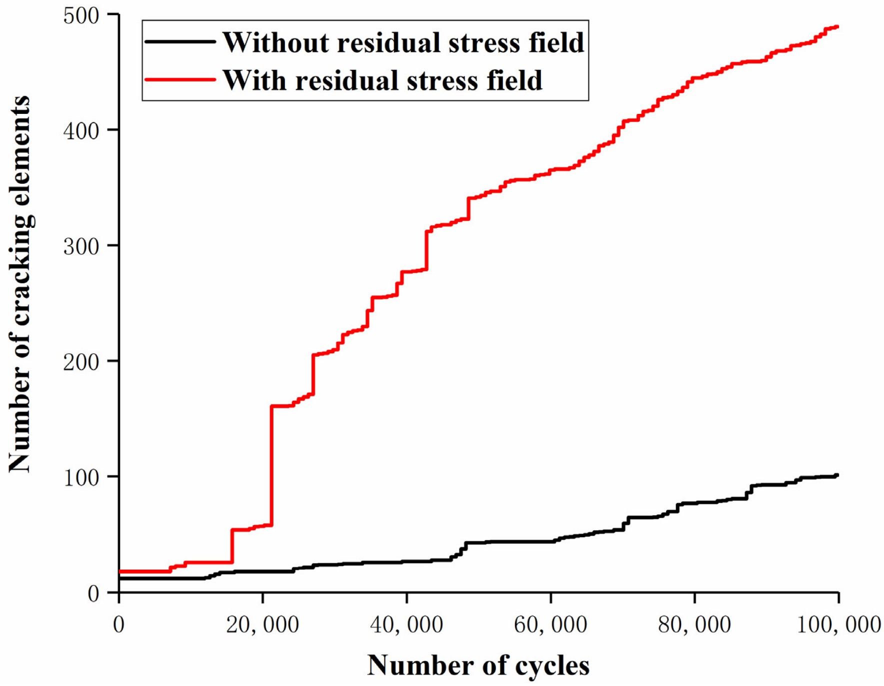

Figure 20. Relationship between the number of cracked elements and number of load cycles for with a maximum displacement load of 0.35 mm.

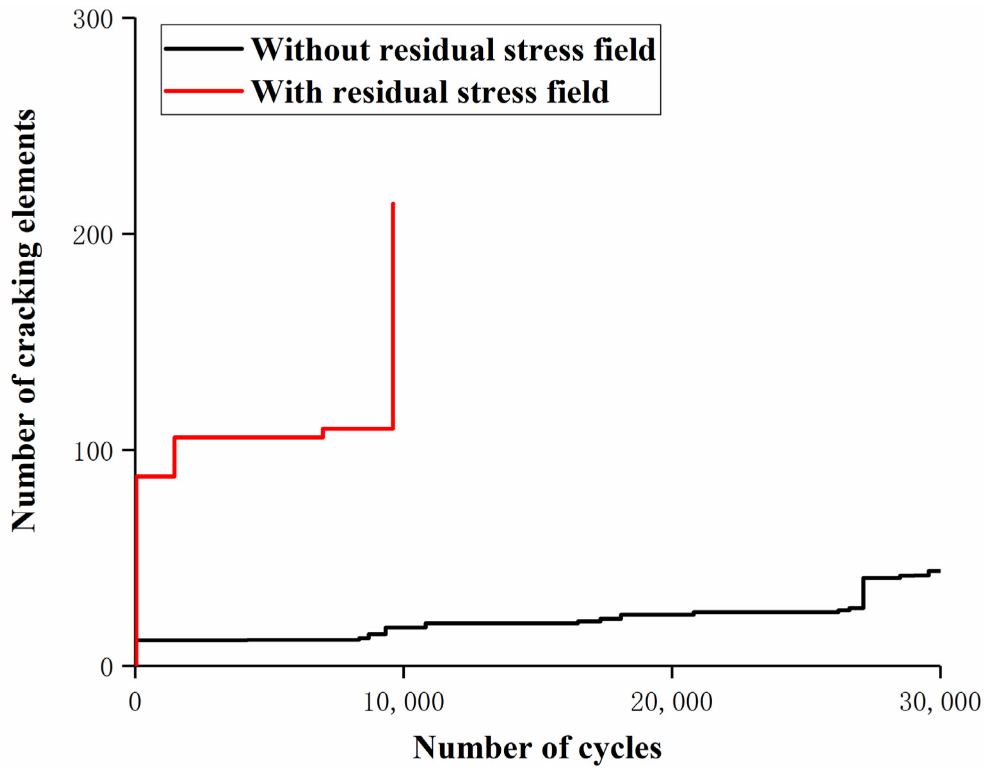

Figure 21. Relationship between the number of cracked elements and number of load cycles for with a maximum displacement load of 0.4 mm.

Under the 0.3 mm displacement load, crack propagation with no residual stress field and with the residual stress field exhibited approximately the same rate below 70,000 cycles; above 70,000 cycles, the crack propagated faster with the residual stress field than without. Furthermore, twice as many elements were eventually damaged by the crack propagation with the residual stress field than without. Under the 0.35 mm maximum displacement load, a significant difference in crack propagation rate was exhibited after only 18,000 cycles, and the final difference in crack propagation rate was five-fold. Indeed, it can be observed that the residual stress field accelerated the crack propagation rate, and this trend is more noticeable under large loading displacements. Under the 0.4 mm displacement load, crack propagation with the residual stress field damaged more than 200 elements after only 9618 cycles, whereas crack propagation without the residual stress field damaged only 50 elements after 30,000 cycles. Under the 0.5 mm displacement load, crack propagation with the residual stress field expanded to damage more than 400 elements after only 37 cycles, tens of times faster than that without the residual stress field. Indeed, the rate and direction of the crack propagation changed owing to the tensile residual stresses in the weld area; the residual stress field deflected crack propagation into the web in both the longitudinal and thickness directions and resulted in a propagation rate several to tens of times faster than that without the residual stress field.

4.2. Effect of Residual Compression Stress

Figure 22 shows the distribution of the maximum absolute values of the three principal residual stresses. An element is shown as black if the principal stress corresponding to the maximum absolute value of three principal stresses is compressive. It can be observed that the previous crack propagation analysis remained in the residual tensile stress region.

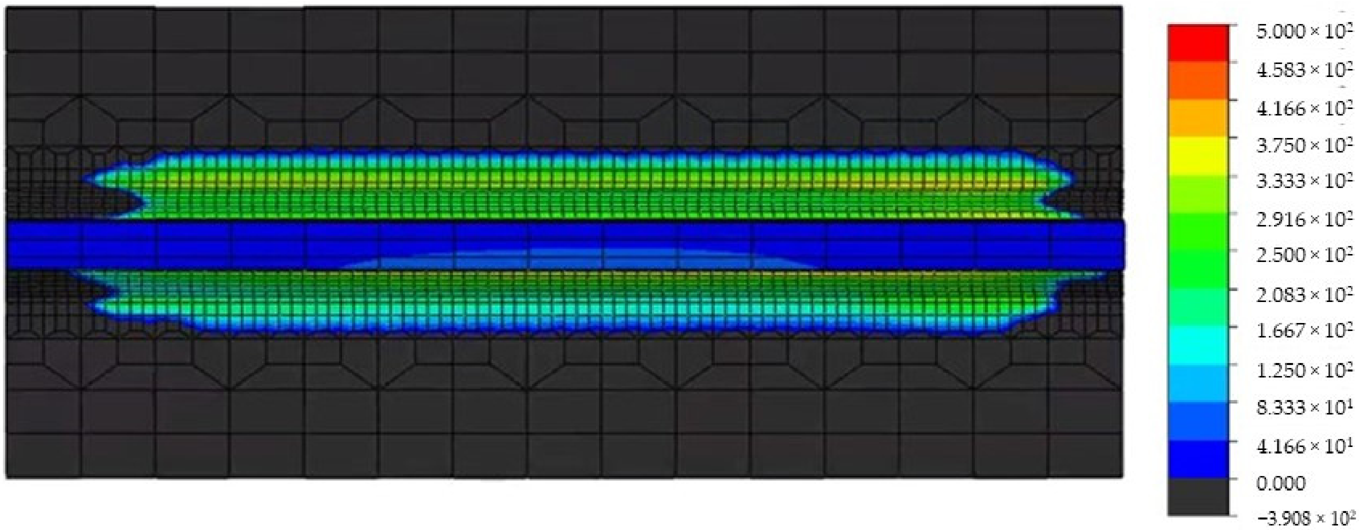

Figure 22. Main principal stress cloud of residual stress (unit: MPa).

The initial crack was therefore placed in the residual compressive stress region at either the start or end of the weld joint in order to study the influence of residual compressive stress on crack propagation. The maximum displacement of the cyclic load was 0.35 mm, and the initial crack size was shown as in Figure 14. The crack propagation patterns in the length and thickness directions with and without the residual stress field are shown in Figures 23 and 24 for the cracks in the start and end of the weld, respectively.

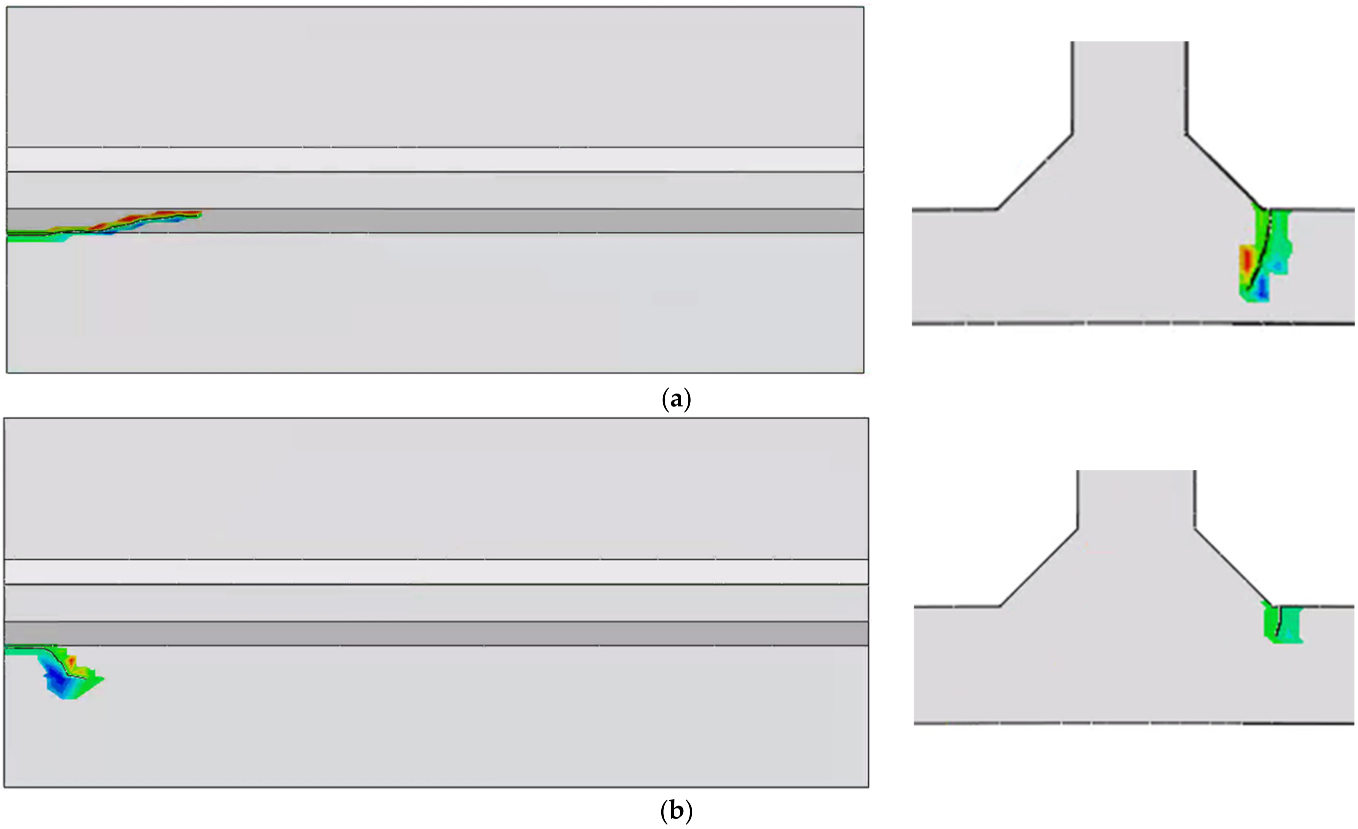

Figure 23. Crack propagation under a maximum displacement load of 0.35 mm when the initial crack is located in the start of the weld: (**a**) without a residual stress field at 81,566 cycles; (**b**) with residual stress field at 100,000 cycles.

(**a**)

(**b**)

Figure 24. Crack propagation under a maximum displacement load of 0.35 mm when the initial crack is located in the end of the weld: (**a**) without a residual stress field at 100,000 cycles; (**b**) with residual stress field at 100,000 cycles.

It can be observed that without a residual stress field, the crack at either end propagated along the weld length direction, though there was a tendency to propagate to the web. The previous scenario indicated that under the influence of residual tensile stress, the crack propagating along the length direction began to propagate in the web direction. However, in the present scenario, the crack propagated outward under the influence of residual compressive stress. In the thickness direction, when there was no residual compressive stress, the crack basically propagated vertically downward, while it hardly propagated in the thickness direction under the influence of residual compressive stress. Furthermore, crack length did not obviously increase under the influence of the residual tensile stress, even in the thickness direction, whereas it decreased under the influence of residual compressive stress.

The numbers of damaged elements according to the applied cycle count are shown in Figures 25 and 26 to approximate the crack propagation rate. Under any number of cycles, the number of cracking elements without residual compressive stress was always greater than that with residual compressive stress, whether the crack was initiated in the start or end of the weld. Particularly for the crack in the start of the weld, the larger the number of cycles, the greater is the gap between the number of damaged elements without residual compressive stress than with residual compressive stress. Contrary to the previous influence of residual tensile stress on the crack growth rate, under the influence of residual compressive stress, the crack growth rate does not accelerate or even decrease. In other words, residual compressive stress can slow down crack growth.

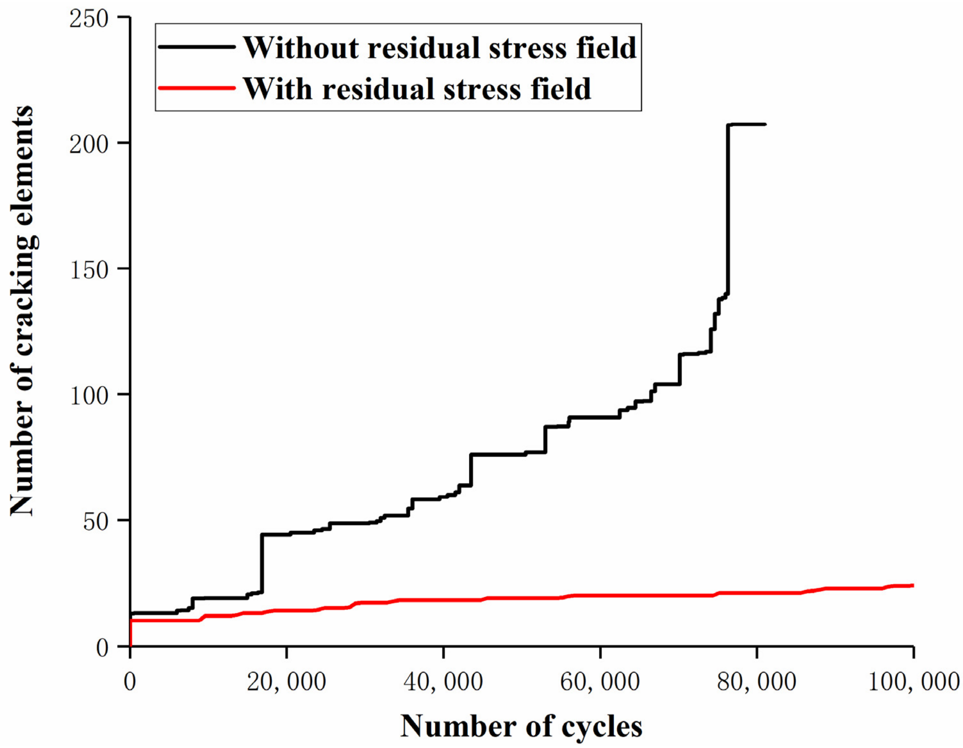

Figure 25. Crack expansion rate when the initial crack is located at the start of the weld.

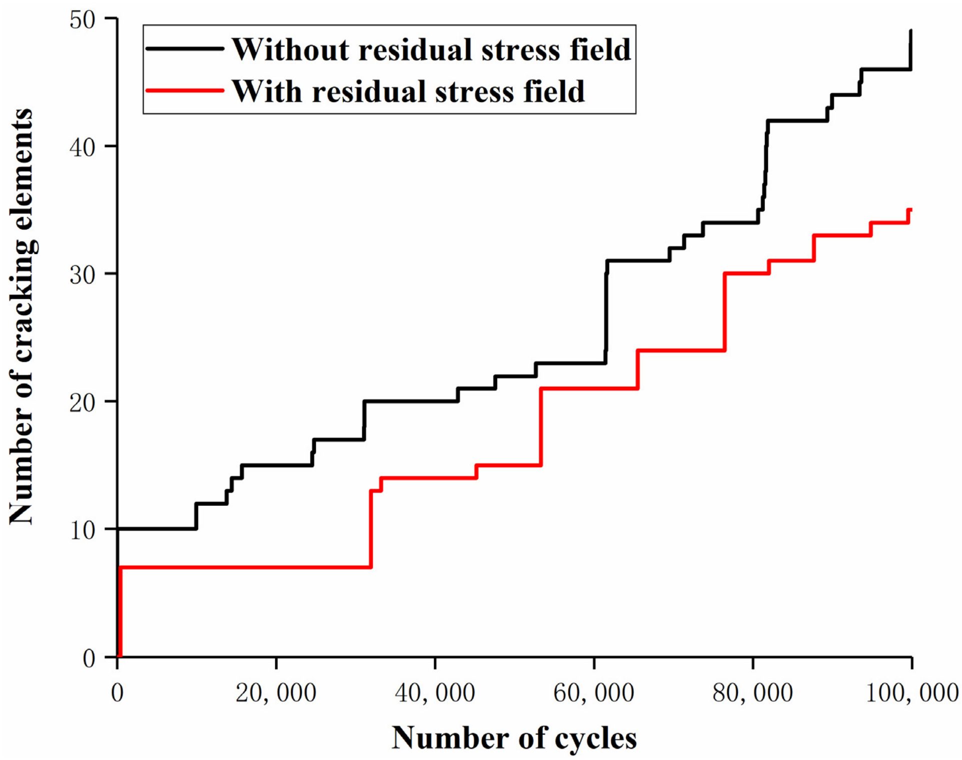

Figure 26. Crack expansion rate when the initial crack is located at the end of the weld.

4.3. Effects of Three Principal Residual Stresses on Crack Propagation

In this section, the three principal stresses of the complete residual stress field were individually evaluated to further explore the effect of residual stress on crack propagation.

The distributions of tensile and compressive stress in the X, Y, Z directions are shown in Figure 27. The colour distribution of tensile and compressive stresses is similar to those in Figure 22.

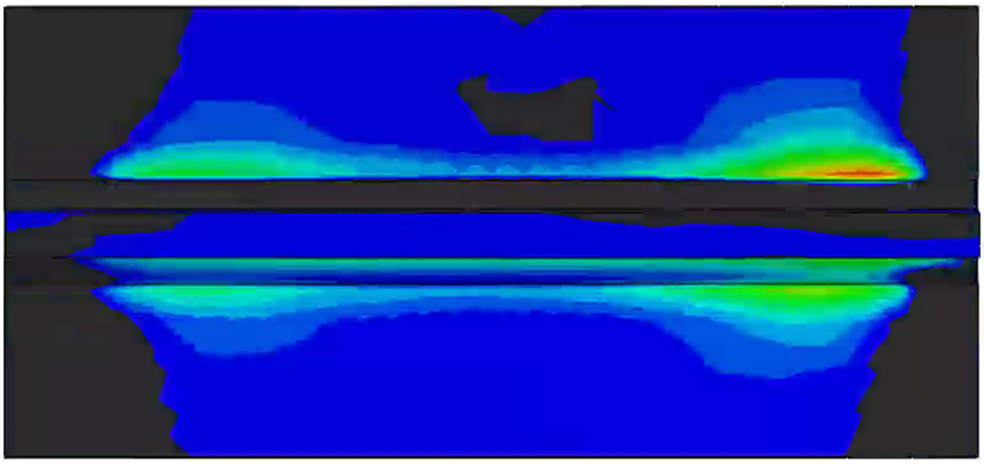

(**a**)

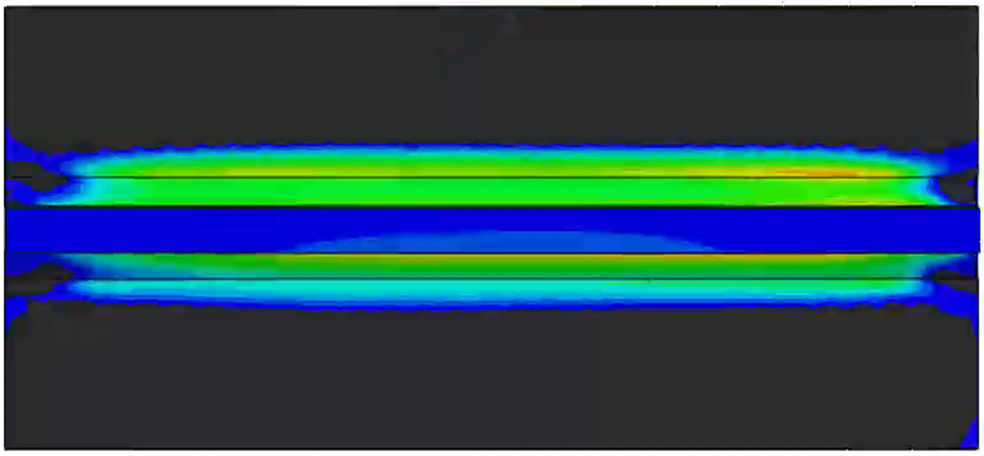

(**b**)

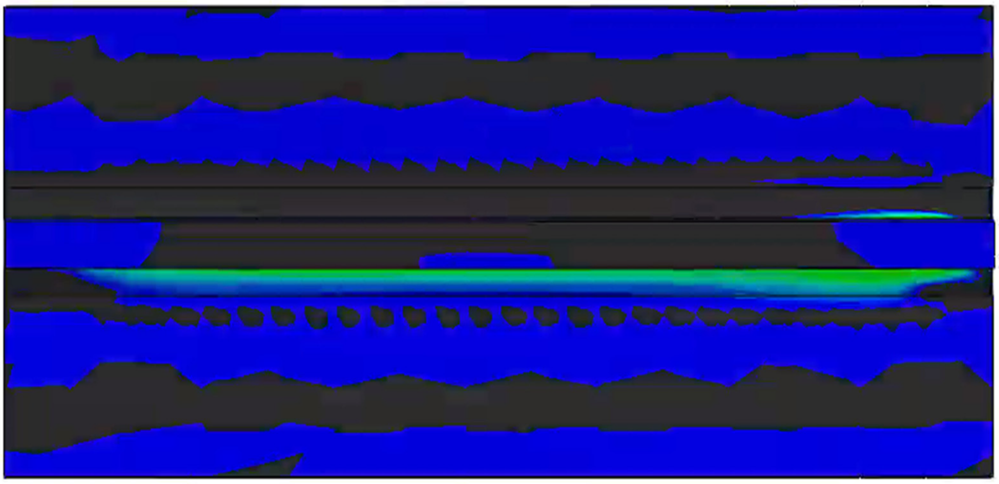

(**c**)

Figure 27. Tensile and compressive stress distribution: (**a**) X-directional; (**b**) Y-directional; (**c**) Z-directional.

The maximum cyclic load displacement was set to 0.35 mm. As the initial crack was placed in the middle of the first weld (Figure 14), all residual stresses in the X, Y, and Z directions were tensile. The crack propagation rates are shown in Figure 28, which indicates that when the number of cycles reached the maximum, more elements were damaged when considering the residual stresses in the X, Y, or Z directions than without considering them because the initial crack was located in a region of tensile residual stress no matter the direction. The residual stress in the Y direction (weld length direction) had the least effect on the crack growth rate because it was parallel to the initial crack direction. The residual stresses in the X and Z directions had considerable influence on the crack growth rate because these stresses acted perpendicular to the initial crack length direction, thereby applying a force pulling the crack open. However, compared with the crack propagation under the complete residual stress (Figure 20), the effects of the individual X, Y and Z direction stresses on the crack propagation rate were not notable.

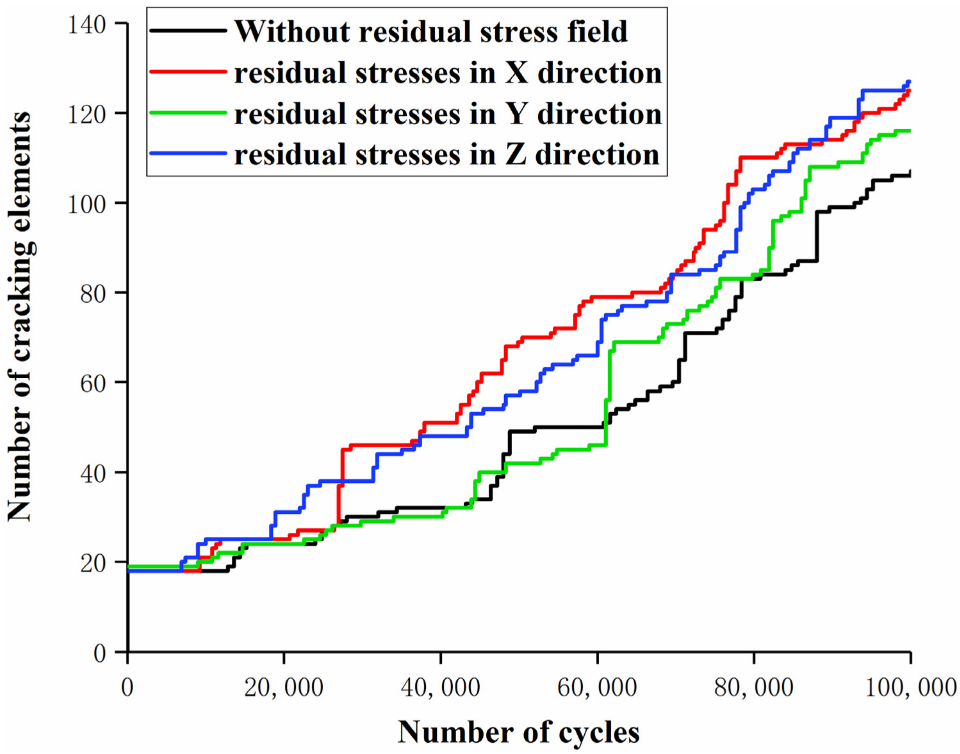

Figure 28. Crack expansion rate under the influence of anisotropic residual stress.

Therefore, the influence of residual tensile stress on crack propagation in T-joint welded joints is a result of the combined effect of multiple directions of residual stresses, rather than a single dominant principal stress.

5. Conclusions

In this study, fracture mechanics theory and the XFEM were applied to numerically simulate fatigue crack extension in a T-joint. Using the sequential coupling method, the temperature and residual stress fields of the T-joint were successively simulated and verified against existing test results. After confirming that reliable residual stress fields were obtained, fatigue crack propagations with and without residual stress fields were compared. The following conclusions can be drawn based on the results of this analysis.

- During the welding process, a large residual tensile stress is induced at the weld toe of the T-joint, the value of which is close to the yield strength of the base material, providing the basis for fatigue crack propagation.

- The presence of the residual stress field was observed to shift the crack in the length and depth directions towards the web and accelerate its propagation. The crack propagation rate increased twofold at a displacement loading of 0.3 mm and tens of times at a displacement loading of 0.5 mm.
- The effect of residual stress on the direction and rate of crack propagation was more pronounced at large displacement loads and low-cycle fatigue loads. Therefore, the effect of residual stress should be carefully considered when evaluating the fatigue properties of T-joints, subjected to large displacement and low-cycle fatigue.

Author Contributions: Conceptualization, S.C.; methodology, M.G.; formal analysis, M.G.; data curation, M.G.; writing—review and editing, Y.L.; visualization, X.D. and M.G.; supervision, S.C.; project administration, J.H.; funding acquisition, J.H. All authors have read and agreed to the published version of the manuscript.

Funding: This study was supported by National Natural Science Foundation of China (Grant No. 51708226, 51638009, 51808357).

Institutional Review Board Statement: Not applicable.

Informed Consent Statement: Not applicable.

Data Availability Statement: Not applicable.

Conflicts of Interest: The authors declare no conflict of interest.

References

1. Belytschko, T.; Black, T. Elastic crack growth in finite elements with minimal remeshing. *Int. J. Numer. Methods Eng.* **1999**, *45*, 601–620. [CrossRef]
2. Giner, E.; Sukumar, N.; Denia, F.; Fuenmayor, F. Extended finite element method for fretting fatigue crack propagation. *Int. J. Solids Struct.* **2008**, *45*, 5675–5687. [CrossRef]
3. Singh, I.V.; Mishra, B.; Bhattacharya, S.; Patil, R. The numerical simulation of fatigue crack growth using extended finite element method. *Int. J. Fatigue* **2012**, *36*, 109–119. [CrossRef]
4. Bhattacharya, S.; Sharma, K. Fatigue crack growth simulations of FGM plate under cyclic thermal load by XFEM. In *Proceedings of the Structural Integrity*; Jayakumar, T., Sandhya, R., Rao, B.P.C., Bhaduri, A.K., Eds.; Elsevier Science Bv: Amsterdam, The Netherlands, 2014; Volume 86, pp. 727–731.
5. Zhang, J.; Hertele, S.; Micone, N.; De Waele, W. Modelling framework for 3d fatigue crack propagation in welds of offshore steel structures. In *Proceedings of the Irf2016: 5th International Conference Integrity-Reliability-Failure*; Gomes, J.F.S., Meguid, S.A., Eds.; Inegi-Inst Engenharia Mecanica E Gestao Industrial: Porto, Portugal, 2016; pp. 751–762.
6. Ooi, G.T.C.; Roy, S.; Sundararajan, S. Investigating the effect of retained austenite and residual stress on rolling contact fatigue of carburized steel with XFEM and experimental approaches. *Mater. Sci. Eng. A* **2018**, *732*, 311–319. [CrossRef]
7. Solob, A.; Grbović, A.; Božić, Ž.; Sedmak, S. XFEM based analysis of fatigue crack growth in damaged wing-fuselage attachment lug. *Eng. Fail. Anal.* **2020**, *112*, 104516. [CrossRef]
8. Ebrahimi, S.H. Residual stress effects on crack-tip stress singularity in XFEM fracture analysis. *Eur. J. Mech. A/Solids* **2020**, *86*, 104191. [CrossRef]
9. Perić, M.; Nižetić, S.; Garašić, I.; Gubeljak, N.; Vuherer, T.; Tonković, Z. Numerical calculation and experimental measurement of temperatures and welding residual stresses in a thick-walled T-joint structure. *J. Therm. Anal.* **2020**, *141*, 313–322. [CrossRef]
10. Pilipenko, A. *Computer Simulation of Residual Stress and Distortion of Thick Plates in Multielectrode Submerged Arc Welding: Their Mitigation Techniques*; Fakultet for ingeniørvitenskap og teknologi: Trondheim, Norway, 2001; ISBN 978-82-471-5340-6.
11. Perić, M.; Tonković, Z.; Rodić, A.; Surjak, M.; Garašić, I.; Boras, I.; Švaić, S. Numerical analysis and experimental investigation of welding residual stresses and distortions in a T-joint fillet weld. *Mater. Des.* **2014**, *53*, 1052–1063. [CrossRef]
12. Liu, C.; Zhang, J.; Xue, C. Numerical investigation on residual stress distribution and evolution during multipass narrow gap welding of thick-walled stainless steel pipes. *Fusion Eng. Des.* **2011**, *86*, 288–295. [CrossRef]
13. Pavelic, V.; Tanbakuchi, R.; Uyehara, O.A.; Myers, P.S. Experimental and computed temperature histories in gas tungsten-arc welding of thin plates. *Weld. J.* **1969**, *48*, 296–305.
14. Pan, J.; Chen, S.; Lai, Z.; Wang, Z.; Wang, J.; Xie, H. Analysis and fracture behavior of welded box beam-to-column connections considering residual stresses. *Constr. Build. Mater.* **2017**, *154*, 557–566. [CrossRef]
15. Deng, D. FEM prediction of welding residual stress and distortion in carbon steel considering phase transformation effects. *Mater. Des.* **2009**, *30*, 359–366. [CrossRef]
16. Schenk, T. Modelling of Welding Distortion; the Influence of Clamping and Sequencing. Ph.D. Thesis, Delft University of Technology, Materials Science and Engineering, Delft, The Netherlands, 2011.

17. Benzeggagh, M.L.; Kenane, M. Measurement of mixed-mode delamination fracture toughness of unidirectional glass/epoxy composites with mixed-mode bending apparatus. *Compos. Sci. Technol.* **1996**, *56*, 439–449. [CrossRef]
18. Sukumar, N.; Huang, Z.Y.; Prévost, J.-H.; Suo, Z. Partition of unity enrichment for bimaterial interface cracks. *Int. J. Numer. Methods Eng.* **2004**, *59*, 1075–1102. [CrossRef]
19. Paris, P. A Critical Analysis of Crack Propagation Laws. *J. Basic Eng.* **1963**, *85*, 528–533. [CrossRef]
20. Nagy, W. Fatigue Assessment of Orthotropic Steel Decks Based on Fracture Mechanics. Ph.D. Thesis, Ghent University, Faculty of Engineering and Architecture, Ghent, Belgium, 2017.
21. Bozkurt, F.; Schmidová, E. Fracture Toughness Evaluation of S355 Steel Using Circumferentially Notched Round Bars. *Period. Polytech. Transp. Eng.* **2018**, *47*, 91–95. [CrossRef]